Icarus 405 (2023) 115713

Contents lists available at ScienceDirect

Icarus

journal homepage: www.elsevier.com/locate/icarus

The SOIR/Venus Express species concentration and temperature database: CO_2, CO, H_2O, HDO, $H^{35}Cl$, $H^{37}Cl$, HF individual and mean profiles

A. Mahieux [a,b,*], S. Robert [a], A. Piccialli [a], L. Trompet [a], A.C. Vandaele [a]

[a] Belgian Institute for Space Aeronomy, Brussels, Belgium
[b] The University of Texas at Austin, Austin, TX, USA

ARTICLE INFO

Keywords:
Venus mesosphere
Composition
Thermal structure
Database
Solar occultation

ABSTRACT

This work is an update of the SOIR mean and individual profiles of CO_2, CO, H_2O, HDO, $H^{35}Cl$, $H^{37}Cl$, HF, and the temperature measured at the Venus terminator during the Venus Express mission (2006–2014).

The previous versions of the database were published by Chamberlain et al. (2020); Mahieux et al. (2015a); Mahieux et al. (2012); Mahieux et al. (2015c); Vandaele et al. (2016a, b). Updates to the pipeline to computing the calibrated transmittances by Trompet et al. (2016) and to the retrieval code led to a new database version.

For each species, we provide the individual profiles and associated uncertainties. We compute the mean profiles and their associated variability of the whole database, the morning and evening profiles for absolute latitudes lower than 60°, and for four latitude bins (0°-30°, 30°-60°, 60°-80°, and 80°-90°) assuming equatorial and side of the terminator symmetry. The mean profiles are compared to the ones of the previously published database and with literature profiles. They are all in good agreement.

The numerical values of the mean profiles are provided in the Appendix of this work, the individual profiles are available on the VESPA platform, and the calibrated transmittances are available on the ESA PSA.

1. Introduction

The Venus mesosphere and lower thermosphere are barely known regions of the Venus atmosphere, extending above the cloud top at ~65 km. Before the arrival of Venus Express in 2006, only a few missions and ground-based instruments had studied the composition and thermal structure of the atmosphere above the clouds (Donahue, 1968; Mills and Allen, 2007; Moroz, 1981; Taylor, 2006).

With the arrival of Venus Express (Marcq et al., 2018; Titov et al., 2006) and the different spectrometers on board the spacecraft (VIRTIS (Drossart et al., 2007), SPICAV-IR and SPICAV-UV (Bertaux et al., 2007a), and SOIR (Nevejans et al., 2006)), the composition and thermal structure of the upper-atmosphere could be studied in more details (Limaye et al., 2017; Limaye et al., 2018; Vandaele et al., 2015, 2016). Many species were targeted by the different instruments, such as H_2O and HDO (Bertaux et al., 2007b; Chamberlain et al., 2020; Cottini et al., 2015; Fedorova et al., 2008; Fedorova et al., 2016; Luginin et al., 2018), CO (Encrenaz et al., 2020; Encrenaz et al., 2015; Gilli, 2012; Gilli et al., 2015; Tsang et al., 2009; Vandaele et al., 2015, 2016; Vandaele et al., 2015), HCl and HF (Bertaux et al., 2007b; Krasnopolsky et al., 2013; Mahieux et al., 2015c; Sandor and Clancy, 2012; Sandor and Clancy, 2017), SO_2 (Belyaev et al., 2016; Belyaev et al., 2017; Encrenaz et al., 2016; Encrenaz et al., 2020; Encrenaz et al., 2015; Jessup et al., 2015; Oschlisniok et al., 2021), O_3 (Montmessin et al., 2011), OCS (Arney et al., 2014; Krasnopolsky, 2010a; Marcq et al., 2008; Marcq et al., 2018), and the temperature (Limaye et al., 2017; Limaye et al., 2018; Mahieux et al., 2015a; Piccialli et al., 2015; Tellmann et al., 2012).

More particularly, the SOIR instrument studied the Venus terminator from solar occultation measurements. This paper presents an update of previous publications (Chamberlain et al., 2020; Mahieux et al., 2015a; Mahieux et al., 2012; Mahieux et al., 2015c; Vandaele et al., 2015, 2016) regarding the chemical composition and thermal structure of the Venus mesosphere and lower-thermosphere at the terminator and all latitudes, following an update of the spectral calibration pipeline by Trompet et al. (2016).

All the SOIR data presented here are available on the Virtual European Solar and Planetary Access (VESPA) at the address https://vespa-client-dev.obspm.fr/planetary/data/ and are described in Trompet et al. (2018).

* Corresponding author at: Belgian Royal Institute for Space Aeronomy, Brussels, Belgium.
E-mail address: arnaud.mahieux@aeronomie.be (A. Mahieux).

https://doi.org/10.1016/j.icarus.2023.115713
Received 22 June 2023; Received in revised form 19 July 2023; Accepted 19 July 2023
Available online 24 July 2023
0019-1035/© 2023 The Author(s). Published by Elsevier Inc. This is an open access article under the CC BY-NC-ND license (http://creativecommons.org/licenses/by-nc-nd/4.0/).

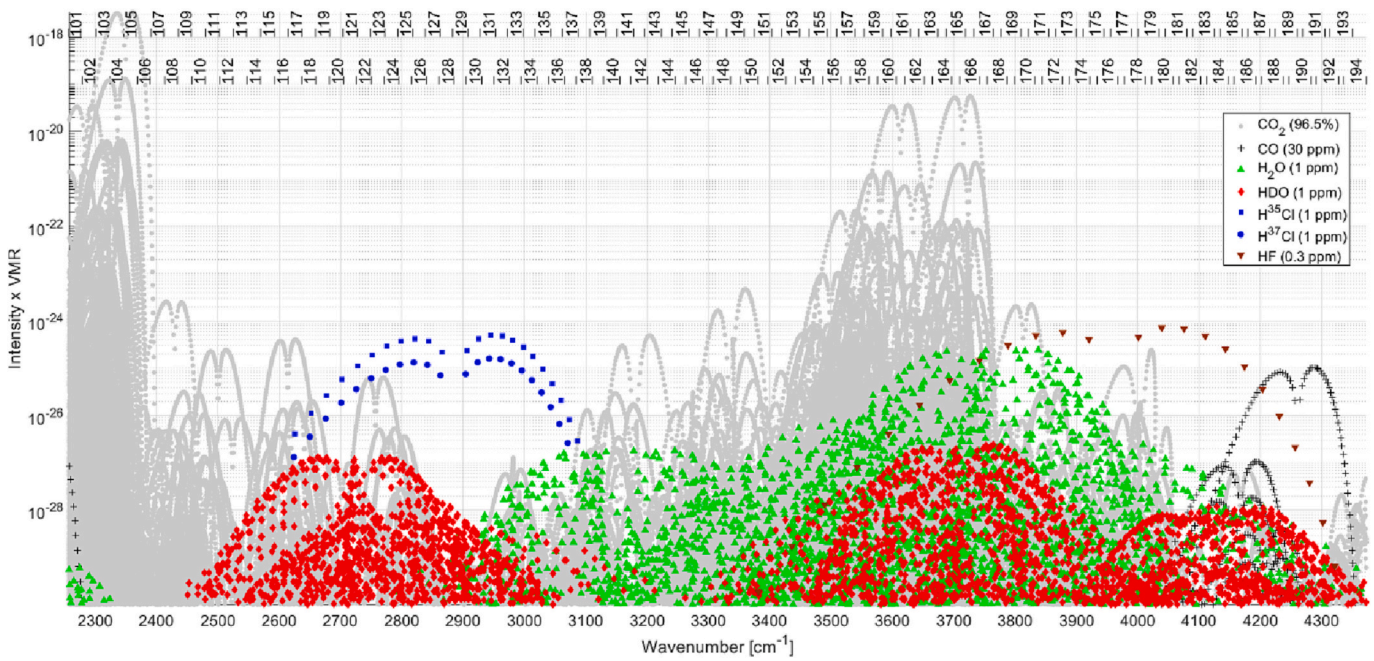

Fig. 1. Position and intensity of the CO_2 and CO (and isotopologues), H_2O, HDO, $H^{35}Cl$, $H^{37}Cl$, and HF lines from HITRAN 2012 (Rothman et al., 2013), multiplied by typical Venus mesosphere volume mixing ratios (VMR), given in the legend. The order boundaries are given at the top of the figure.

2. The SOIR instrument on board Venus Express

2.1. Instrument description

SOIR was an echelle-grating infrared (IR) spectrometer on board the Venus Express (VEx) spacecraft operating exclusively in Solar Occultation (SO) mode. A thorough description of the instrument can be found in Mahieux et al. (2008); Mahieux et al. (2012); Nevejans et al. (2006), and a summary will be reported here.

VEx was following a polar elliptical orbit whose period was equal to 24 h, with its perigee above the North Pole at altitudes between 250 and 450 km and the apogee above the South Pole at altitudes between 45,000 and 65,000 km (Titov et al., 2006). The VEx orbit plane was rotating relative to the Venus-Sun axis, with a period of ~1.5 Earth months.

SOIR was operating in the near-IR between 2.2 and 4.4 μm (2200 to 4400 cm^{-1}). The spectral range was divided into 94 diffraction orders – simply called orders in the following – ranging from 101 to 194. The instrument resolving power was equal to 20,000. The detector counted 320 pixels in its spectral direction and 24 illuminated pixels in its spatial direction. Because of telemetry limitations between VEx and the Earth, the pixel lines in the spatial direction needed to be binned in two spatial bins. The pixel spectral resolution varied between 0.06 and 0.12 cm^{-1} with increasing order. The order to be measured could be selected thanks to an Acousto Optical Tunable Filter (AOTF), which was located on the instrument's optical path right after the entrance slit, whose transfer function (TF) had a shape close to a sinc-squared, with a full-width at half maximum close to the free spectral range of the echelle grating (~24 cm^{-1}). The AOTF TF is studied in detail in Mahieux et al. (2009), which provides the relation between the crystal radio frequency and the desired wavenumber/order and how the AOTF TF shape varies with the orders. Because of the side lobes of the AOTF TF, the three adjacent orders on both sides of the targeted order were leaking on the detector; thus, to correctly build a synthetic SOIR spectrum, seven orders were taken into account, moduled by the AOTF TF, see Mahieux et al. (2010) for a full description on how to build SOIR spectra.

The SOIR products are transmittances obtained by dividing spectra measured while looking at the Sun through the Venus atmosphere by spectra measured while looking at the Sun just before (or after) the occultation, following an updated procedure described in Trompet et al. (2016). The SOIR typical signal-to-noise (SNR) ratio varied between 500 and 3000. The SOIR slit always pointed at the Sun during an occultation, with the full slit always covered by the Sun disk. The stability of the spacecraft pointing was very high, with pointing errors of the order of 0.2 mrad, corresponding to a few meters at the tangent point in SO mode.

SOIR could measure four different orders per second, thus each order at a 1 Hz cadence, which allowed targeting different species or the same species but in different spectral regions, thus absorbing in different altitude regions. For a given occultation, the SOIR dataset corresponds to eight sets of transmittances, taken at different tangent altitudes, corresponding to the four orders and two spatial bins.

The SOIR-calibrated transmittances are available on ESA's Planetary Science Archive (PSA) at https://www.cosmos.esa.int/web/psa/venus-express.

The vertical sampling – the vertical distance between two observations for a given order and bin – varied between 2 km at the North Pole, 500 m between 40° and 70° North, and up to 5 km at the South Pole, due to the VEx elliptical orbit. The field of view – the size of the projected instrument slit at the measurement point – ranged from 200 m for Northern polar observations to 5 km at the South Pole.

2.2. The SOIR observations

The SOIR spectral dataset corresponds to eight sets of transmittance spectra per occultation. The list of occultations can be found in Table 3 of Appendix B. Usually, four different orders were scanned during an occultation. In a few cases, only one order was targeted with eight spatial bins; in other few cases, two orders were targeted with four spatial bins. In Table 3, for such cases, values of −1 are reported for orders #2, #3, and/or #4. One to two occultations were performed during the VEx orbit when the observation geometry allowed a SO, corresponding to the egress and ingress cases of the occultation. We distinguish between those by adding a decimal to the occultation number; for example, in Table 3, occultations 145.1 and 145.2 occurred on 13 September 2006. The SOs were not always possible during a VEx

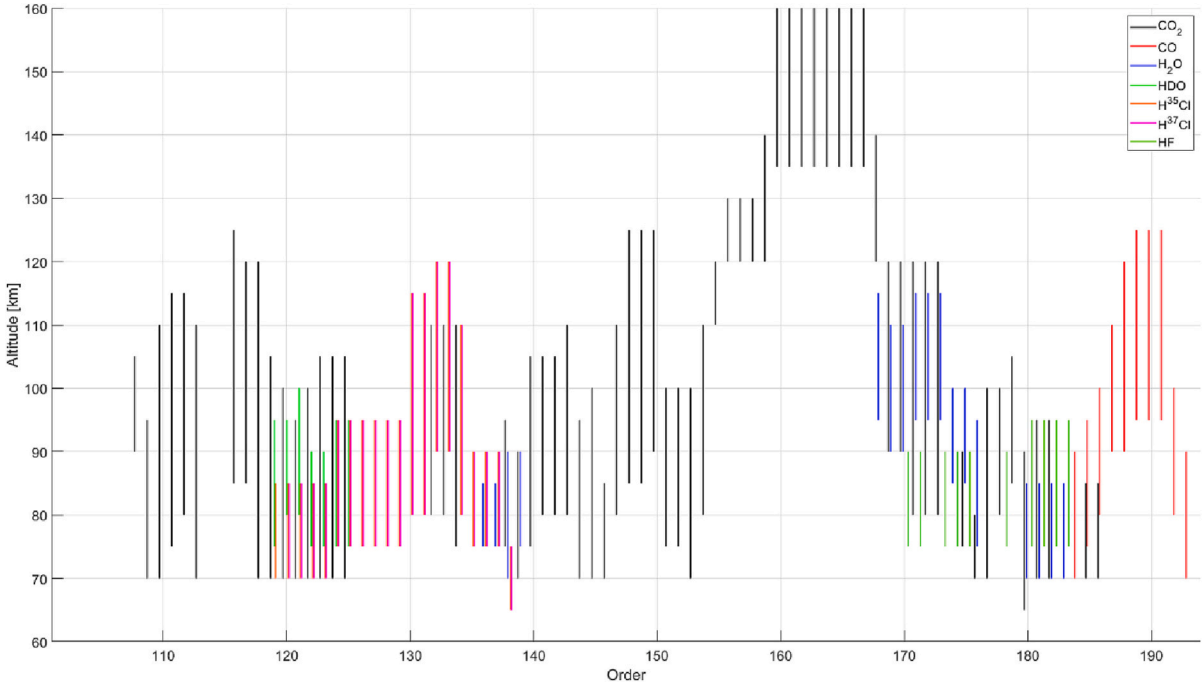

Fig. 2. Typical altitude range for detecting the species in each order. The colour code refers to the species; see the legend.

orbit because of (1) interference with measurements performed by other instruments on board VEx that required an orientation of the satellite that would prevent from having the SOIR boresight from pointing at the Sun and (2) the orbital plane of the VEx spacecraft that was rotating relative to the Venus-Sun axis such that an occultation would not be possible considering the geometry Venus-Sun-VEx.

The orders were selected by choosing which species to target and which altitude range. Hence, considering the observation geometry (i.e. the length of the light path through the atmosphere), the SOIR instrumental characteristics (i.e. the SNR), the strength of the spectral lines, and the Venus International Reference atmosphere (VIRA) (Hedin et al., 1983; Zasova et al., 2006), one can determine the maximum altitude at which the species absorption lines were larger than the noise level. The minimum altitude corresponds to the spectra in which the absorption lines are saturated, corresponding to spectroscopic lines at infinite resolution, i.e., considering the synthetic spectrum before convolution by the instrument resolution, having depths deeper than 0.15 in transmittance. This criterion is set up to ensure that the fitted absorption lines remain in the optically thin regime and thus can be correctly modelled by a Voigt profile. Fig. 1 provides the line position of all the targeted species together with their intensities multiplied by typical VMRs of the Venus mesosphere (96.5% for CO_2, 30 ppm for CO, 1 ppm for $H^{35}Cl$, $H^{37}Cl$, H_2O, and HDO, and 0.3 ppm for HF). The order limits are also provided at the top of the figure. Fig. 2 provides the approximate altitude range in which the different species could be derived in each order. The list of orders considered to derive the number densities of each species is given in Table 2 of Appendix A.

3. The inversion algorithm

3.1. Description

The inversion algorithm, named ASIMAT, is described in Mahieux et al. (2012), Mahieux et al. (2015a), and Mahieux et al. (2015c); a summary is given here.

ASIMAT uses the Bayesian inversion scheme described in Rodgers (2000) in an onion-peeling frame, assuming spherical symmetry of the atmosphere.

For CO_2 retrievals, since it is the major species of the Venus atmosphere, the temperature profile considering the hydrostatic equation is also computed (Mahieux et al., 2015a; Mahieux et al., 2012). An iterative scheme is set up, and each iteration consists of two main steps: (1) the spectral fit of the SOIR spectra and (2) the computation of the temperature profile.

At the first iteration, the CO_2 number density profile is computed from the SOIR transmittance spectra and considering the temperature profile from VIRA. At the end of the iteration, the temperature profile is computed from the fitted CO_2 vertical profile. At the next iteration, a new CO_2 number density profile is fitted on the same transmittances considering the new temperature profile from the previous iteration. Iterations are made until both the CO_2 number density and the temperature profiles remain within the uncertainty of the profiles at the previous step. Convergence usually occurs within three to four steps.

The computation of the CO_2 number density profile is performed as follows. We consider the orders and bins in which CO_2 absorbs for a given occultation. An individual inversion of each set of spectra from each order and bin is performed, using the Bayesian approach of Rodgers (2000), in the altitude range in which the spectral lines are seen out of the instrument noise down to the altitude at which the spectral lines become optically saturated, following the procedure described in Mahieux et al. (2012) and Mahieux et al. (2015a). Then, an analysis of the averaging kernels and the degrees of freedom from the fits is done to extract only the number densities that were actually fitted. The individual number density profiles from the different bins and orders in which CO_2 absorbs are combined using a moving average procedure, weighted by the uncertainties on the individual number density profiles. The outputs from this procedure are the CO_2 number density profiles and their associated uncertainties.

For the other species (CO, H_2O, HDO, HCl, and HF), if CO_2 was measured simultaneously, the temperature profile is taken from the result of that computation; if CO_2 was not simultaneously measured, the temperature profile is taken from the mean profiles given in Mahieux et al. (2015a). Iterations are also made using the same approach as the one described for CO_2, i.e., until the combined number density profiles of two successive iterations lie within the uncertainty of each other, keeping the temperature profile constant.

Table 1
Summary of the observations by targeted species, separated by latitude bin and by side of the terminator, assuming equatorial symmetry.

Species	AM					PM					Total
	0°-30°	30°-60°	60°-80°	80°-90°	Total	0°-30°	30°-60°	60°-80°	80°-90°	Total	
CO_2	72	61	82	127	342	84	56	85	117	342	684
CO	27	29	26	49	131	35	28	35	37	135	266
H_2O	32	40	40	63	175	31	28	38	53	150	325
HDO	33	29	34	48	144	23	17	27	47	114	258
$H^{35}Cl$	42	40	49	79	210	48	28	54	65	195	405
$H^{37}Cl$	38	38	51	77	204	49	26	52	63	190	394
HF	32	32	29	49	142	28	27	38	49	142	284

3.2. Updates to the previous version of the algorithm

The database presented in this work is different from what was published in Mahieux et al. (2015a) for CO_2, in Vandaele et al. (2015, 2016) for CO, and in Mahieux et al. (2015c) for HCl and HF. Though, for H_2O and HDO, the database is the same as in Chamberlain et al. (2020) and Mahieux et al. (2023b).

The changes made to the algorithm are the following:

(1) The transmittance spectra and the corresponding uncertainties are now computed as in Trompet et al. (2016). The changes include a more accurate computation of the uncertainty on the transmittances, accounting for drifts of the signal while looking at the Sun before or after the occultation and discarding problematic occultations during which not enough points were taken before, or the line of sight was crossing the Venus atmosphere. The drift of the signal could be related to a faint limb darkening.
(2) Corrections to the computation of the temperature profile from the fitted CO_2 number density. The integration of the hydrostatic derivative equation is done while setting the upper boundary condition as isothermal (i.e., over the first two points or $\frac{dT}{dz}\big|_{z_{max}} = 0$) instead of using a boundary condition on the temperature.
(3) The information from the averaging kernels and the number of degrees of freedom is used to decide which altitude range of each fit in a given order and bin is to be considered or not. More precisely, after a spectral inversion using the Bayesian algorithm, we compute the number of degrees of freedom related to the number density using the averaging kernel matrix (Rodgers, 2000). We sort the fitted spectra based on their eigenvalues and only consider the number of spectra lower than the degrees of freedom.
(4) More orders were considered for detecting several species; see Table 2 in Appendix A.

4. The SOIR datasets

4.1. Introduction

Seven species had absorption lines that could clearly be seen in the SOIR transmittance spectra, i.e. which have signatures larger than the noise level: CO_2, CO, H_2O, HDO, $H^{35}Cl$, $H^{37}Cl$, and HF.

Other species (SO_2, SO_3, OCS, CS, and CS_2) have a signature that was too weak to be seen out of the noise, and they are derived using a specific statistical technique, see Belyaev et al. (2012); Mahieux et al. (2023); Mahieux et al. (2015b). Mahieux et al. (2023) provide the number densities and VMRs of the targeted species. That paper also provides

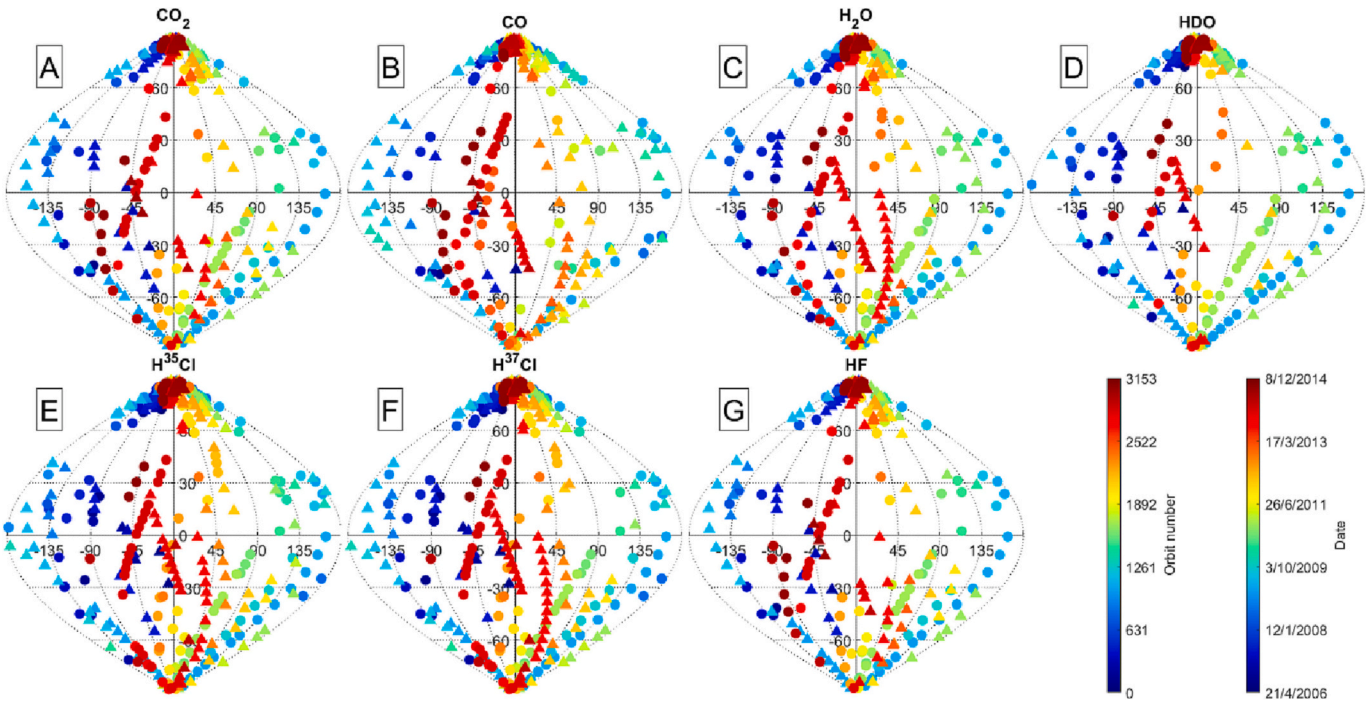

Fig. 3. Location of the SOIR observations separated by species/isotopologues as a function of the latitude and longitude. The colour code is the orbit number/date of the observation (DD/MM/YYYY); see the colour bars at the bottom right. The circles correspond to morning observations, while the triangles correspond to evening observations.

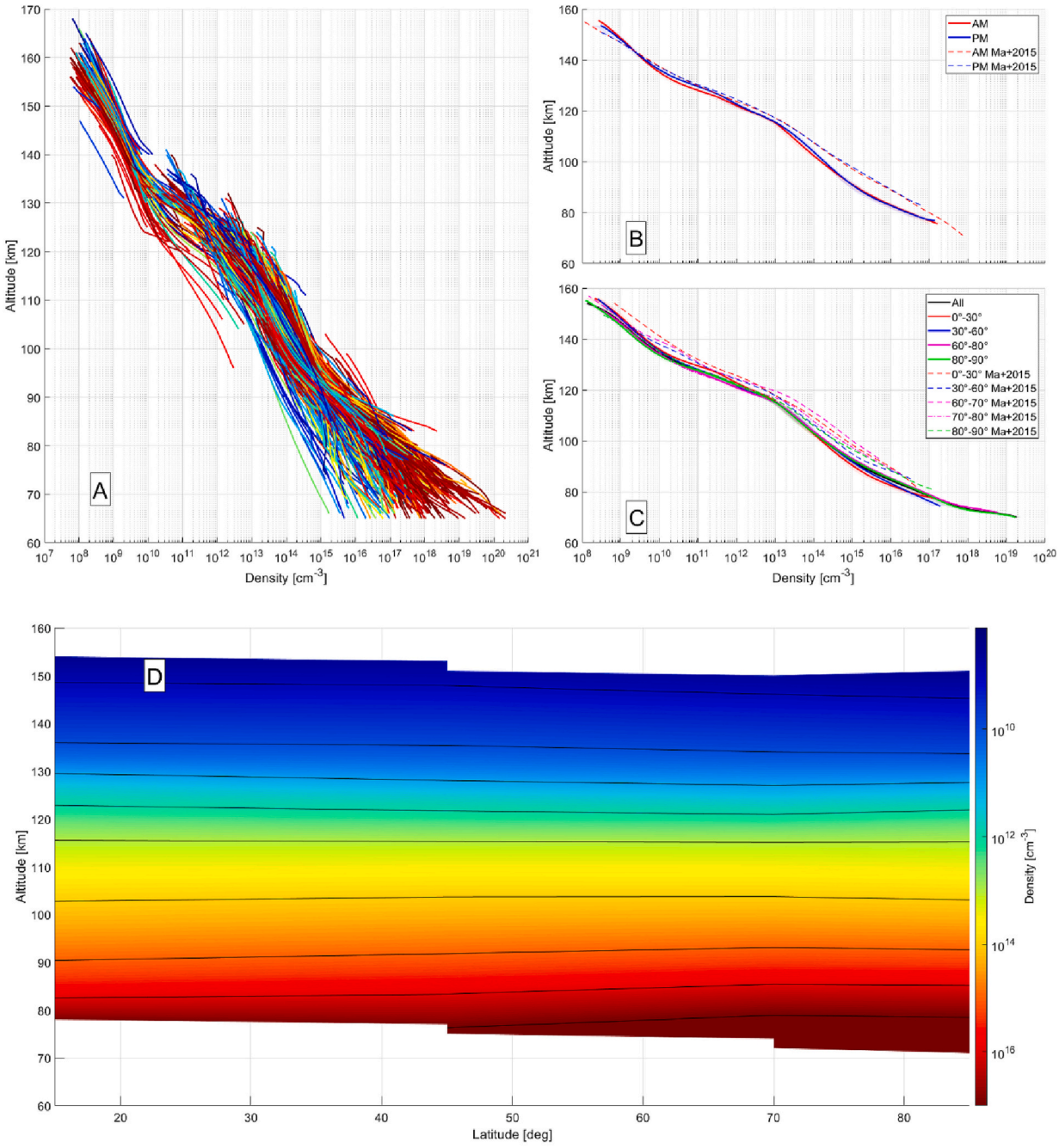

Fig. 4. (Panel A) Individual retrieved CO_2 number density profiles as a function of the altitude. The colour code is the time, from blue for 2006 observations to red for the 2014 ones. (Panel B) Mean CO_2 number density profiles for the morning (red) and evening profiles (blue) for absolute latitudes lower than 60°. (Panel C) Mean CO_2 number density profiles for the whole database (black), for 0°-30° latitude observations (red), 30°-60° (blue), 60°-80° (magenta), and 80°-90° (green). Equatorial symmetry is assumed between the Northern and Southern hemispheres. (Panel D) Map of the mean CO_2 density as a function of the altitude and the absolute latitude. In Panels B and C, the envelopes show the variability, and the mean CO_2 profiles from Mahieux et al. (2015a) are provided. In Panel C, the latitude bin profiles of Mahieux et al. (2015a) are from the morning side of the terminator. (For interpretation of the references to color in this figure legend, the reader is referred to the web version of this article.)

upper limits for H_2S and HOCl.

Table 1 summarises the number of observations of each species by latitude bin assuming equatorial symmetry between the Northern and Southern hemispheres and by side of the terminator. Equatorial symmetry is assumed in the mean profiles by bins of latitudes. No difference between the Northern and Southern hemispheres is supposed to be observed since Venus does not have seasons, and its tilt axis is nearly perpendicular to the ecliptic (177.4°). The location of the observations for each species is summarised in Fig. 3.

The list of orbits and measurement details (date, scanned orders, longitude, latitude, local solar time, and altitude range covered by species) is given in Table 3 of Appendix B, and the numerical values of the mean profiles are in Appendix C Table 4.

4.2. Carbon dioxide

This Section is an update to Mahieux et al. (2015a), describing the CO_2 dataset that had been studied at the time of publication and focused

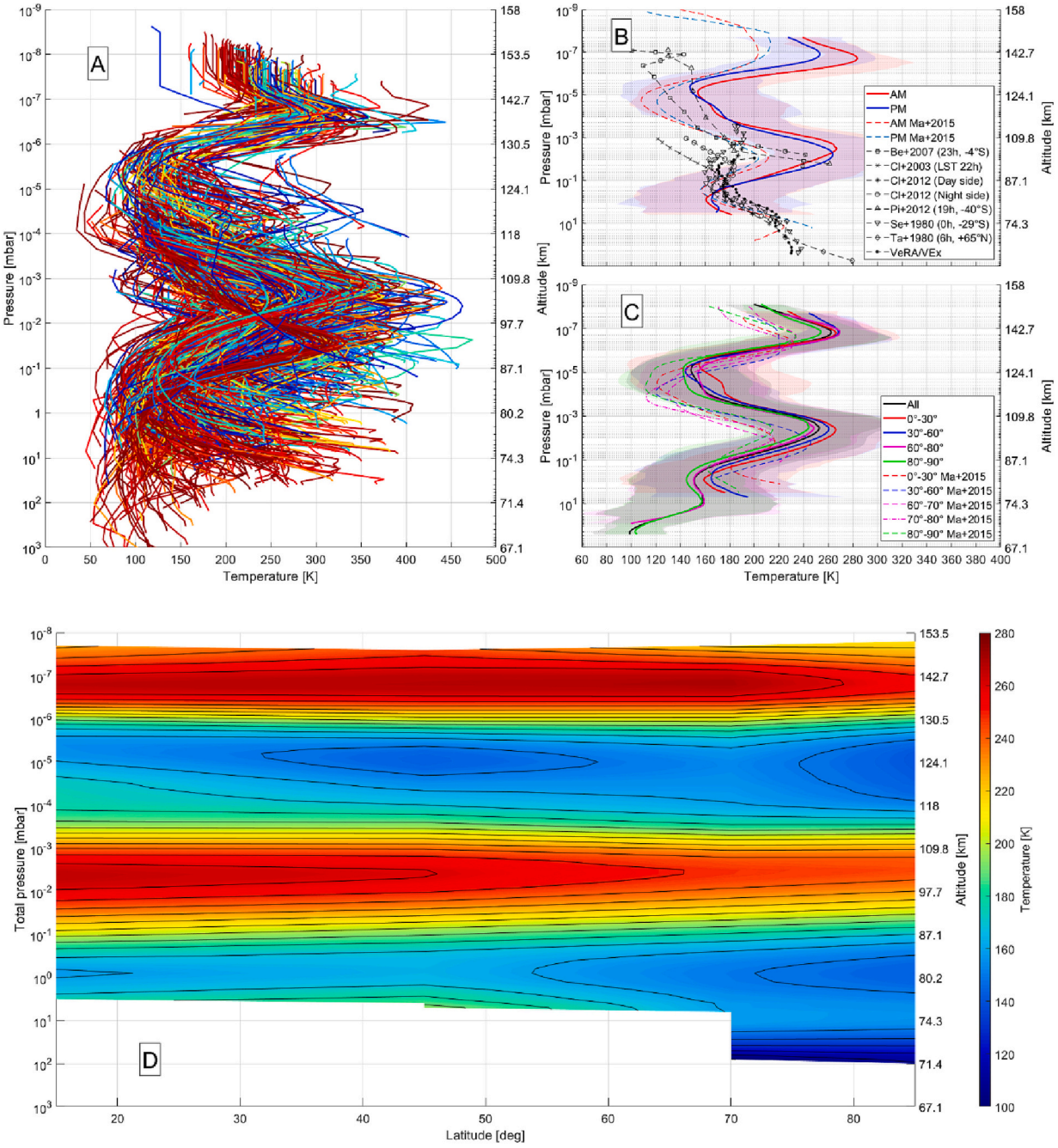

Fig. 5. (Panel A) Individual retrieved temperature profiles as a function of the pressure. The colour code is the time, from blue for 2006 observations to red for the 2014 ones. (Panel B) Mean temperature profiles for the morning (red) and evening (blue). (Panel C) Mean temperature profiles for the whole database (black), for 0°-30° latitude observations (red), 30°-60° (blue), 60°-80° (magenta), and 80°-90° (green). Equatorial symmetry is assumed between the Northern and Southern hemispheres. (Panel D) Map of the mean temperature as a function of the pressure and the absolute latitude. In Panels B and C, the envelopes show the variability, and in Panels B, C, and D, the approximate altitude is given on the right-hand side of the plots. In Panels B and C, the mean profiles from Mahieux et al. (2015a) are provided and referred to in the legend as "Ma + 2015". In Panel B, "Cl + 2003" refers to Clancy et al. (2003), "Cl + 2012" to Clancy et al. (2012), "Pi + 2012" to Piccialli et al. (2012), "Be+2007" to Bertaux et al. (2007b), "Ta + 1980" to Taylor et al. (1980), and "Se+1980" to Seiff et al. (1980).(For interpretation of the references to color in this figure legend, the reader is referred to the web version of this article.)

on 122 SOs.

CO_2 was measured 684 times during the whole VEx mission, covering all latitudes and both sides of the terminator; see Fig. 3 Panel A. It could be derived in the 170 down to 65 km region, covering the thermosphere and mesosphere of Venus. The individual number density profiles are presented in Fig. 4 Panel A, with the colour code being the day of the observations covering the period 22 April 2006 to 8 December 2014, from dark blue to red. The uncertainties on the number densities are not displayed for clarity and vary between 10 and 15% above 140 km, 15 to 40% between 140 and 80 km, and 40 to 60% between 80 and 65 km.

The variability varies with altitude; we compute the weighted standard deviation of the logarithm of the number density profiles on the altitude scale, and it increases from a factor of 0.25 at 162 km to 1.8 at 130 km, decreasing to 0.78 at 95 km, and increasing to 2.9 at 68 km.

Fig. 4 Panel B provides the weighted mean CO_2 number density

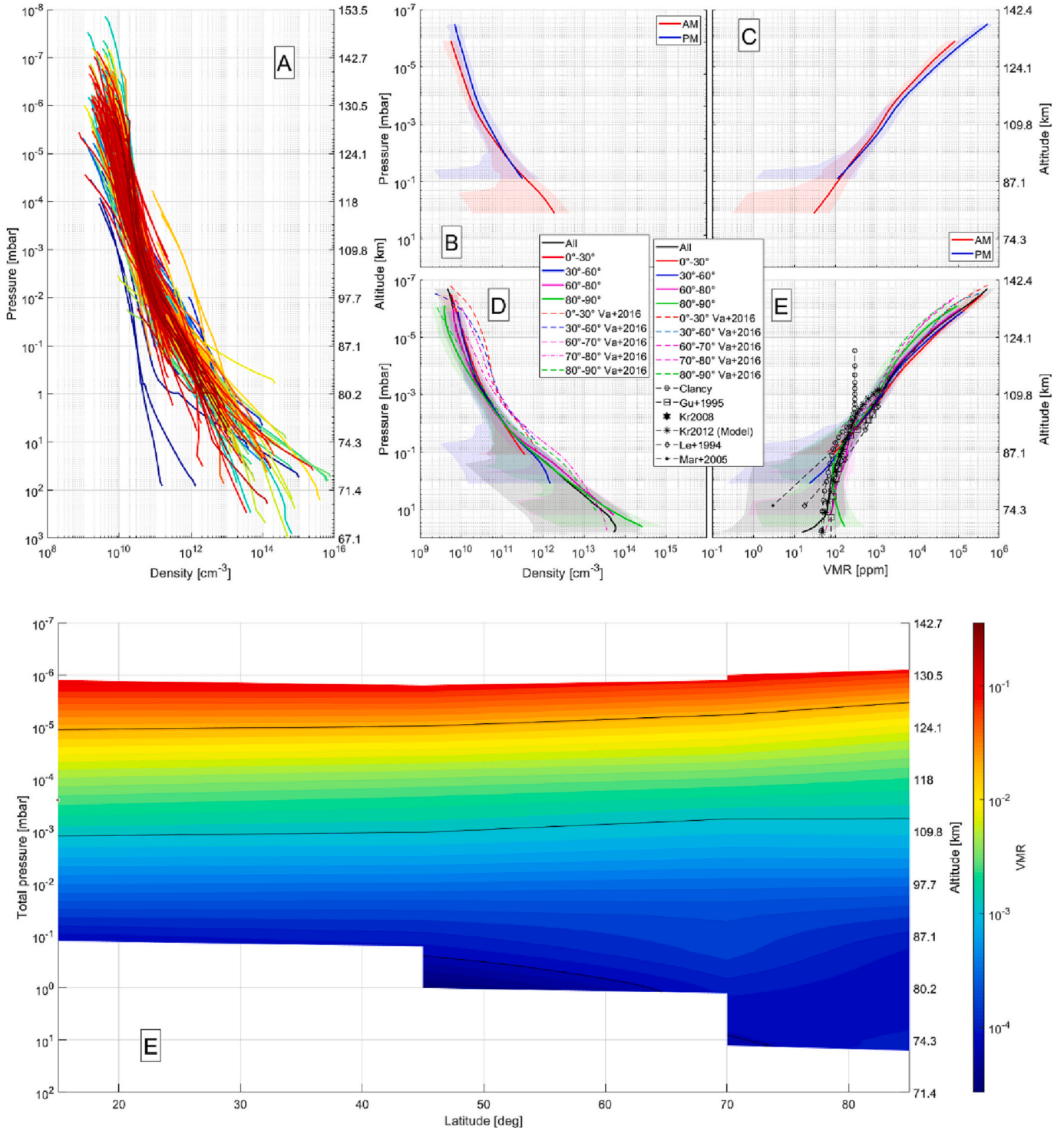

Fig. 6. (Panel A) Individual retrieved CO number density profiles as a function of the altitude. The colour code is the time, from blue for 2006 observations to red for the 2014 ones. (Panel B) Mean CO number density profiles for the morning (red) and evening profiles (blue). (Panel C) Mean VMR of the profiles plotted in Panel B. (Panel D) Mean CO number density profiles for the whole database (black), for 0°-30° latitude observations (red), 30°-60° (blue), 60°-80° (magenta), and 80°-90° (green). Equatorial symmetry is assumed between the Northern and Southern hemispheres. (Panel E) Mean VMR of the profiles plotted in Panel D. (Panel F) Map of the mean CO VMR as a function of the pressure and the absolute latitude. In Panels B and C, the envelopes show the variability, and in Panels C, E, and F, the approximate altitude is given on the right-hand side of the plots. In Panels D and E, the mean latitude bin profiles from Vandaele et al. (2015, 2016) are provided as dashed curves. In Panel E, CO VMR profiles from the literature are also displayed for comparison, with "Clancy" referring to the private communication from Vandaele et al. (2015, 2016), "Gu + 1995" to Gurwell et al. (1995), "Kr2008" to Krasnopolsky (2008), "Kr2012" to the results of the model of Krasnopolsky (2012), "Le+1994" to Lellouch et al. (*1994*), and "Mar + 2005" to Marcq et al. (*2005*).(For interpretation of the references to color in this figure legend, the reader is referred to the web version of this article.)

profiles computed on a pressure scale and displayed as a function of the mean altitude. Only morning and evening observations taken at absolute latitudes lower than 60° are considered. The variability, also computed on a pressure scale and displayed on a mean altitude scale, is presented as coloured envelopes. The limitation to latitudes between −60° and 60° is justified because the local solar time becomes meaningless at high polar latitudes. The maximum difference between the AM and PM profiles is equal to 16% at 132 km, and this value decreases with altitude.

Fig. 4 Panel C displays the weighted mean CO_2 number density profiles as a function of the mean altitude. They are computed on a pressure scale for different latitude bins (0°-30°, 30°-60°, 60°-80°, and 80°-90°), assuming equatorial symmetry, and the variability given as the coloured envelopes, which are computed on the pressure scale. The mean CO_2 profiles are also presented in Panel D as a map. Small systematic variations of the CO_2 density are observed as a function of the latitude: above 130 km, there is a weak trend of the CO_2 density decreasing with increasing latitude, with a shift by −3 km between the Equator and the Poles. An opposite trend is observed below 100 km, with a shift of +3 km between the Equator and the Poles.

The mean CO_2 profiles from Mahieux et al. (2015a) are also plotted as the dashed profiles using the same colour code in Panel B for the morning and evening sides of the terminator and Panels C for the AM latitude bins of that previous work. There is a difference up to an order of magnitude with the previous version. The explanations for these differences are listed in Section 4.2. On top of this, a much larger database is considered in this work compared to Mahieux et al. (2015a), which makes the statistics more reliable.

4.3. Temperature

This Section is an update to the temperature profile study of Mahieux et al. (2015a). Here, we consider the whole SOIR temperature database that contains 684 vertical profiles instead of 122 in that paper. The location of the observations is given in Fig. 3 Panel A.

As explained in Section 4, the hydrostatic temperature was derived together with the CO_2 number density. The individual profiles are plotted in Fig. 5 Panel A on a pressure scale, with the colour code being the day of the observation during the VEx mission, from dark blue to red. The uncertainties are not displayed for clarity; they vary between 10 and 20 K above 140 km, 20 to 40 K in the 140 to 80 km altitude range and 40 and 80 K below 80 km.

The mean profiles for the morning and evening observations are plotted in Fig. 5 Panel B. Only observations taken at latitudes lower than 60° are considered to compute those mean profiles. The mean profiles for four latitude bins (0°-30°, 30°-60°, 60°-80°, and 80°-90°) are given in Panel C. Finally, a map of the mean temperature as a function of the latitude and pressure is given in Panel D. All are given on a pressure scale to remove the large variability observed in the mesosphere and thermosphere, which is reflected in the CO_2 profiles of Fig. 4 Panel A. In Fig. 5 Panels B and C, the coloured envelopes show the variability corresponding to the 1-σ standard deviations of the temperature profiles at each pressure level. The mean AM and PM profiles of Mahieux et al. (2015a) are provided in Panel B as the dashed curves, and the mean latitudinal profiles for the AM observations are given in Panel C. The temperature profiles from previous works (Bertaux et al., 2007b; Clancy et al., 2012; Clancy et al., 2003; Piccialli et al., 2012; Seiff et al., 1980; Taylor et al., 1980) are also presented in Panel B.

Starting from the top of the profiles, a succession of maxima and minima is observed in the mean profile of the whole database given in Panel C: a maximum at 10^{-7} mbar/∼143 km at 262 ± 40 K (mean value and 1-σ standard deviation), a minimum at 10^{-5} mbar/∼124 ± 47 km at 149 K, a maximum at 3×10^{-3} mbar/∼104 km at 253 ± 58 K, and a local minimum at 1 mbar/∼80 km at 151 ± 53 K.

The mean profiles for the two sides of the terminator have the same structure as the mean profile, with different temperatures at the peaks. The maximum difference is found at 10^{-6} mbar/∼130 km and is equal to 44 K; the evening profile is generally cooler than the morning one, except in the 10^{-4} mbar/∼118 km, 10^{-2} mbar/∼98 km, and 1 mbar/∼80 km regions.

Notable differences in the temperature profiles are also observed above the 1 mbar/∼80 km in Panel C while considering the latitude variations. First, the polar profile (80°-90°) is always cooler than the other profiles by 4 to 13 K. The subpolar profile (60°-80°) is cooler than the mean profile in the 10^{-4} mbar/118 km to 10 mbar/∼74 km region up to 7 K and warmer above up to 12 K. Finally, the mid-latitudes (30°-60°) and equatorial (0°-30°) profiles are always warmer than the mean profile, up to 9 K and 22 K, respectively.

Below the 1 mbar/∼80 km level, the mid-latitude and equatorial profiles become much warmer than the subpolar and polar profiles – up to 37 K compared to the mean profile; we observe a clear divergence between the two categories of profiles. Moreover, below the 5 mbar/∼77 km level, data are only available from occultations taken at absolute latitudes larger than 60°, reflected in the mean profile. Panel D shows a map of the mean temperature as a function of latitude and the pressure that reflects this characteristic of the SOIR database.

The mean temperature profiles presented in this work differ from those of Mahieux et al. (2015a); see the dashed temperature profiles in Panels B and C. Since the CO_2 number density profiles differ between the two versions of the dataset, the pressure levels of the peaks are unequal. Moreover, the amplitudes of the peaks are also altered, generally warmer than what was presented in Mahieux et al. (2015a). The new profiles provide temperature values deeper in the atmosphere down to 250 mbar/∼68 km instead of 2 mbar/∼80 km, but only in the polar and subpolar regions. These differences between the two versions of the database can be explained by several facts, such as (1) updates in the retrieval algorithm ASIMAT, see Section 4.2, (2) the much larger database that is considered in this work, and (3) updates in the computation of the transmittances that was described in Trompet et al. (2016).

In Panel B, the mean AM and PM temperature profiles are compared to some temperature profiles from the literature. One typical example of a temperature profile from Bertaux et al. (2007b) is displayed, which was taken in stellar occultation mode by SPICAV-UV/VEx on the Venus nightside (at an LST of 23 h) and close to the Equator (−3°S). The values are within the 1-σ variability of this work's profiles up to 10^{-6} mbar/∼131 km and cooler above. The Clancy et al. (2003) profile, measured using the JCMT ground-based telescope, was also taken on the night side and agrees with the SOIR mean values up to 3×10^{-2} mbar/∼92 km, much cooler above. Thus, it does not reproduce the 3×10^{-3} mbar/∼104 km warm layer, probably because of the LST difference between both observations. The Clancy et al. (2012) dayside and nightside profiles were measured with the same instrument and showed the same behaviours, being cooler in the 3×10^{-2} mbar/∼92 km to 10^{-3} mbar/∼110 km. The Piccialli et al. (2012) profile was obtained from SPICAV-UV/VEx, close to the terminator on the nightside at a latitude of −40°S, and is very similar to the Bertaux et al. (2007b) one, but with a better agreement with this work's mean profiles. The Seiff et al. (1980) was measured by a Pioneer Venus descent probe taken at midnight and −29°S latitude, and is in good agreement with the SOIR dataset up to 3×10^{-2} mbar/∼92 km, cooler above, similar to the Clancy et al. (2012) profiles. Finally, the Taylor et al. (1980) profile measured by an IR spectrometer on board Pioneer Venus agrees with the SOIR data on the whole altitude range.

4.4. Carbon monoxide

This section is an update to Vandaele et al. (2016); Vandaele et al. (2015), which studied 218 profiles of the SOIR database. In this work, we provide a study of the full SOIR database, listing the 266 CO observations. The location of the observations is given in Fig. 3 Panel B.

The individual CO number density profiles are presented in Fig. 6 Panel A, where the colour code is the time of the measurement, from dark blue (2006) to red (2014). The uncertainties are not displayed for

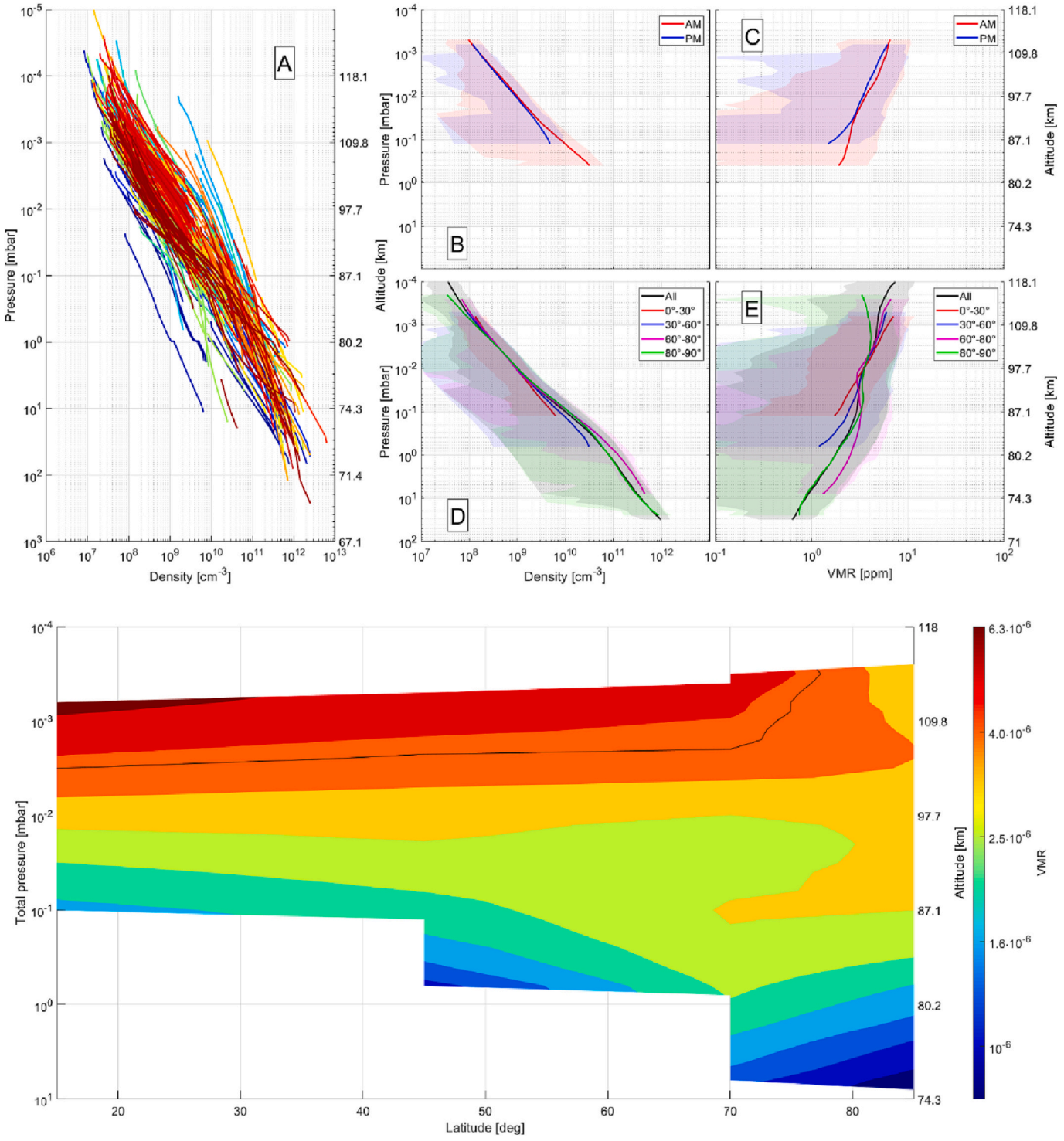

Fig. 7. (Panel A) Individual retrieved H_2O number density profiles as a function of the altitude. The colour code is the time, from blue for 2006 observations to red for the 2014 ones. (Panel B) Mean H_2O number density profiles for the morning (red) and evening profiles (blue). (Panel C) Mean VMR of the profiles plotted in Panel B. (Panel D) Mean H_2O number density profiles for the whole database (black), for 0°-30° latitude observations (red), 30°-60° (blue), 60°-80° (magenta), and 80°-90° (green). Equatorial symmetry is assumed between the Northern and Southern hemispheres. (Panel E) Mean VMR of the profiles plotted in Panel D. (Panel F) Map of the mean H_2O VMR as a function of the pressure and the absolute latitude. In Panels B and C, the envelopes show the variability, and in Panels C, E, and F, the approximate altitude is given on the right-hand side of the plots.(For interpretation of the references to color in this figure legend, the reader is referred to the web version of this article.)

clarity; they vary from 20% at 140 km to 7% at 110 km and increase to 32% at 80 km. The profiles are plotted on a pressure scale to remove the large variations observed in the atmosphere.

The variability, computed as the 1-σ standard deviation of the logarithm of the number density profiles on the pressure scale, varies between factors of 0.2 to 0.5 in the region located above the 10^{-2} mbar/~98 km level and increases linearly up to a factor 3 at 22 mbar/~73 km.

The mean number density profiles as a function of the side of the

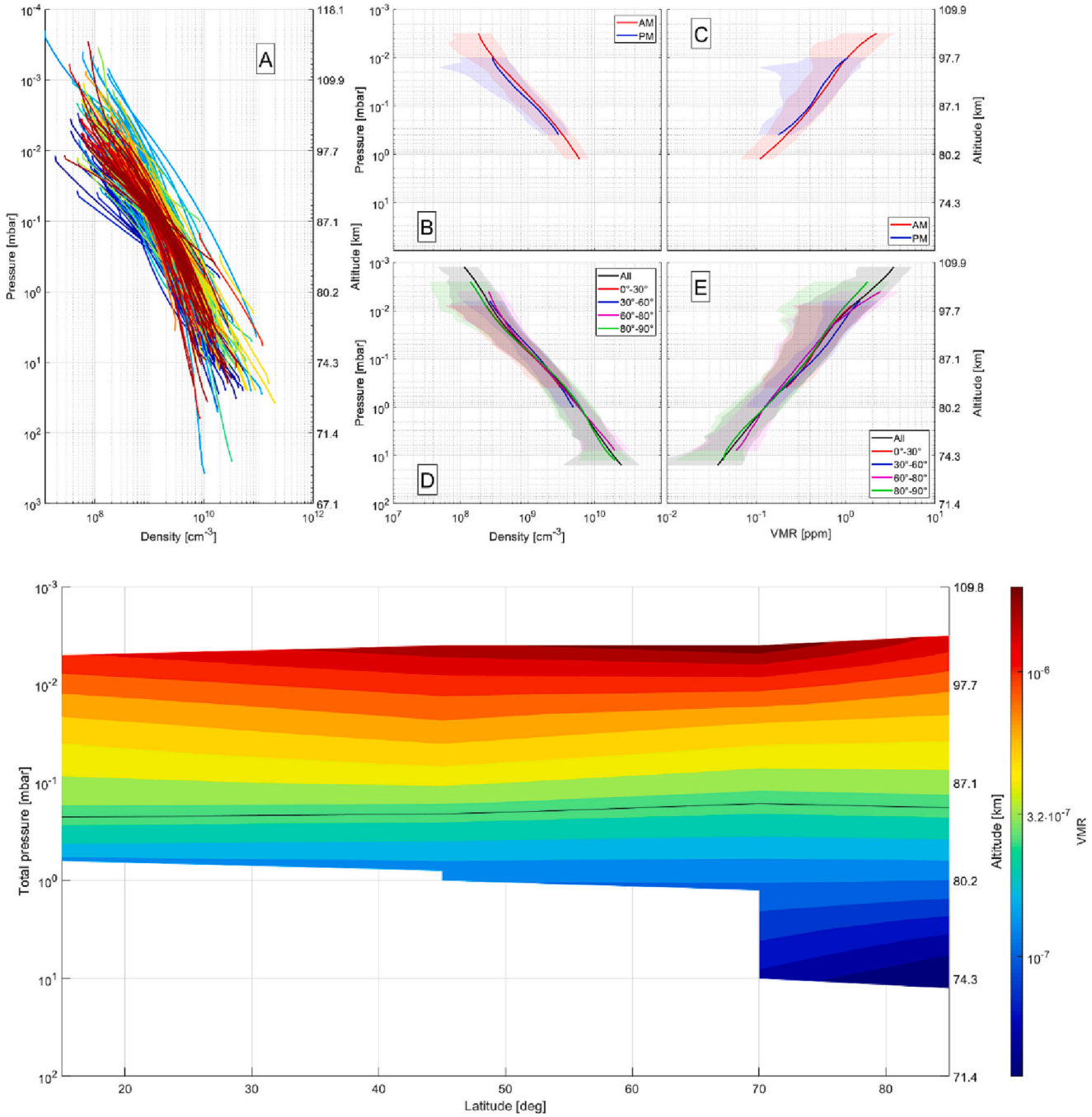

Fig. 8. (Panel A) Individual retrieved HDO number density profiles as a function of the altitude. The colour code is the time, from blue for 2006 observations to red for the 2014 ones. (Panel B) Mean HDO number density profiles for the morning (red) and evening profiles (blue). (Panel C) Mean VMR of the profiles plotted in Panel B. (Panel D) Mean HDO number density profiles for the whole database (black), for 0°-30° latitude observations (red), 30°-60° (blue), 60°-80° (magenta), and 80°-90° (green). Equatorial symmetry is assumed between the Northern and Southern hemispheres. (Panel E) Mean VMR of the profiles plotted in Panel D. (Panel F) Map of the mean HDO VMR as a function of the pressure and the absolute latitude. In Panels B and C, the envelopes show the variability, and in Panels C, E, and F, the approximate altitude is given on the right-hand side of the plots.(For interpretation of the references to color in this figure legend, the reader is referred to the web version of this article.)

terminator are plotted in Fig. 6 Panel B, and the corresponding VMR profiles are given in Panel C. Only occultations occurring between −60° and 60° latitude were considered. In all Panels, the coloured envelopes show the 1-σ variability computed from the standard deviation of the logarithm of the profiles on a pressure scale. There are differences between the AM and PM profiles: the evening profile shows larger VMRs than the morning one by 37% at 10^{-6} mbar/∼131 km. They have equal VMRs at 0.02 mbar/∼100 km, and the evening profile becomes smaller at lower altitudes, up to 20% at 0.08 mbar/∼88 km.

Panels D (number densities) and E (VMRs) give the mean profiles for different latitude bins. Panel F provides a map (latitude vs pressure) of the mean CO VMR. Latitudinal trends are observed. Above the 10^{-2} mbar/∼98 km level, the CO VMR decreases from the Equator to the Pole. At 10^{-6} mbar/∼130 km, there is a reduction by 25% of the CO VMR in the subpolar latitude bin (60°-80°) compared with the equatorial (0°-30°) and mid-latitude (30°-60°) bins and by 52% for the polar bin (80°-90°). At 10^{-4} mbar/∼118 km, the reduction compared to the equatorial bin is by 24% for the mid-latitude bin, 39% for the subpolar

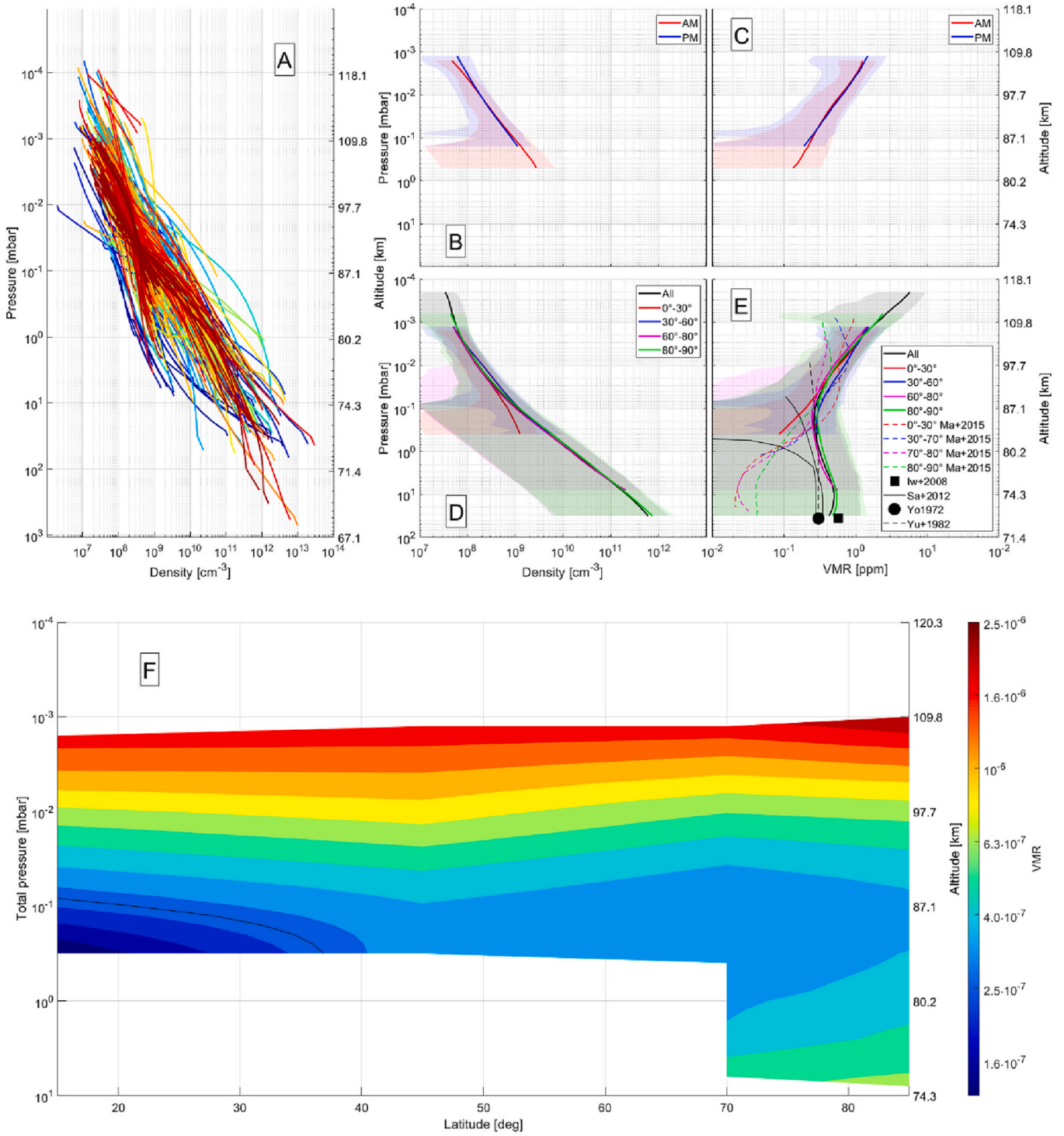

Fig. 9. (Panel A) Individual retrieved $H^{35}Cl$ number density profiles as a function of the altitude. The colour code is the time, from blue for 2006 observations to red for the 2014 ones. (Panel B) Mean $H^{35}Cl$ number density profiles for the morning (red) and evening profiles (blue). (Panel C) Mean VMR of the profiles plotted in Panel B. (Panel D) Mean $H^{35}Cl$ number density profiles for the whole database (black), for 0°-30° latitude observations (red), 30°-60° (blue), 60°-80° (magenta), and 80°-90° (green). Equatorial symmetry is assumed between the Northern and Southern hemispheres. (Panel E) Mean VMR of the profiles plotted in Panel D. (Panel F) Map of the mean $H^{35}Cl$ VMR as a function of the pressure and the absolute latitude. In Panels B and C, the envelopes show the variability, and in Panels C, E, and F, the approximate altitude is given on the right-hand side of the plots. In Panel E, the VMR profiles for the different latitude bins from the previous work of Mahieux et al. (2015c) are also presented. Vertical profiles from the literature are also displayed: "Iw + 2008" corresponds to Iwagami et al. (2008), "Sa + 2012" to Sandor and Clancy (2012), "Yo1972" to Young (1972), and "Yu + 1982" to Yung and DeMore (1982). All literature profiles are multiplied by the $H^{35}Cl$ isotopic ratio (0.7576). (For interpretation of the references to color in this figure legend, the reader is referred to the web version of this article.)

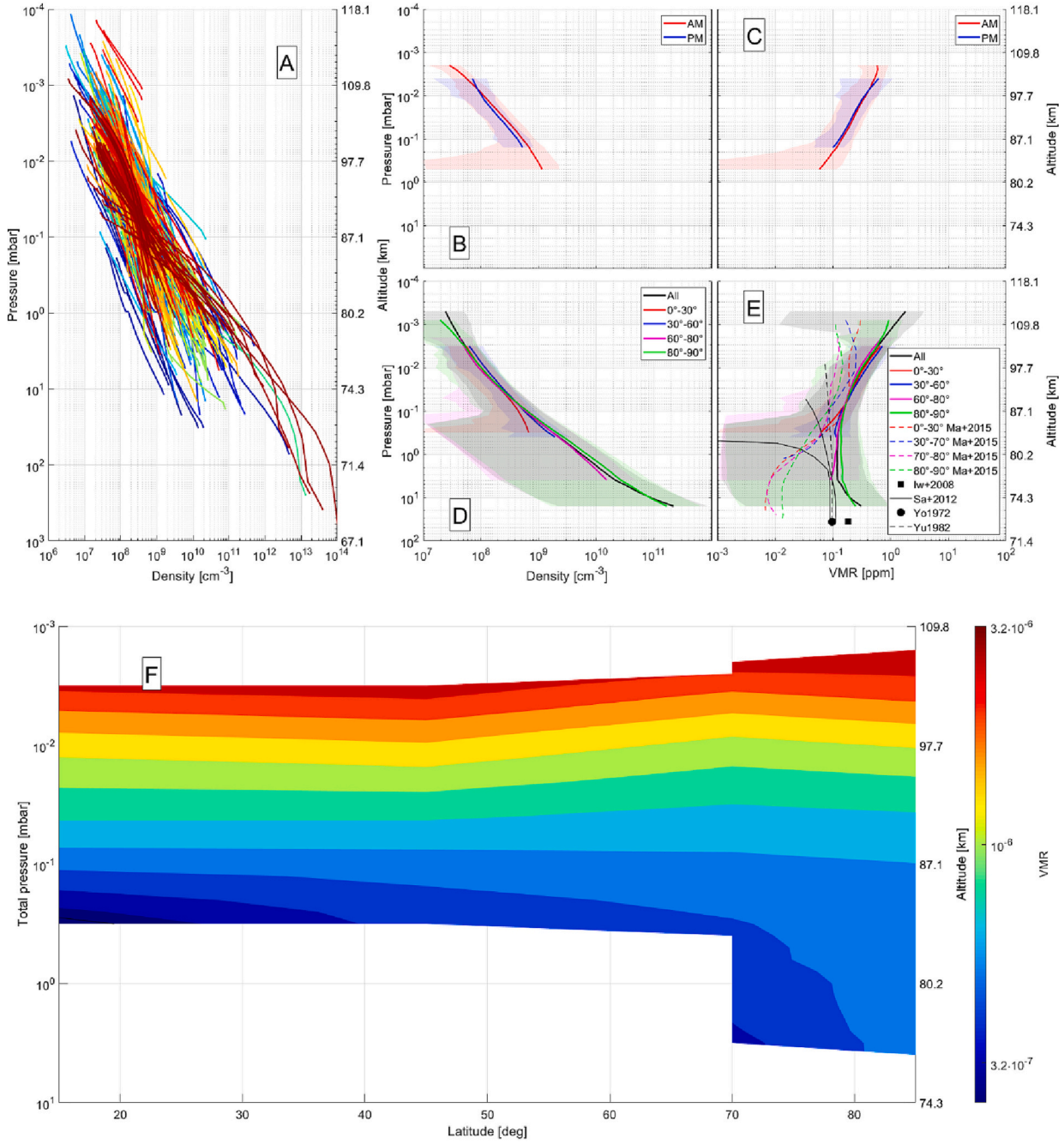

Fig. 10. (Panel A) Individual retrieved $H^{37}Cl$ number density profiles as a function of the altitude. The colour code is the time, from blue for 2006 observations to red for the 2014 ones. (Panel B) Mean $H^{37}Cl$ number density profiles for the morning (red) and evening profiles (blue). (Panel C) Mean VMR of the profiles plotted in Panel B. (Panel D) Mean $H^{37}Cl$ number density profiles for the whole database (black), for 0°-30° latitude observations (red), 30°-60° (blue), 60°-80° (magenta), and 80°-90° (green). Equatorial symmetry is assumed between the Northern and Southern hemispheres. (Panel E) Mean VMR of the profiles plotted in Panel D. (Panel F) Map of the mean $H^{37}Cl$ VMR as a function of the pressure and the absolute latitude. In Panels B and C, the envelopes show the variability, and in Panels C, E, and F, the approximate altitude is given on the right-hand side of the plots. In Panel E, the VMR profiles for the different latitude bins from the previous work of Mahieux et al. (2015c) are also presented. Vertical profiles from the literature are also displayed: "Iw + 2008" corresponds to Iwagami et al. (2008), "Sa + 2012" to Sandor and Clancy (2012), "Yo1972" to Young (1972), and "Yu + 1982" to Yung and DeMore (1982). All literature profiles are multiplied by the $H^{37}Cl$ isotopic ratio (0.2423). (For interpretation of the references to color in this figure legend, the reader is referred to the web version of this article.)

bin, and 51% for the polar bin. A change of regime is observed below the 10–2 mbar/~98 km level (Vandaele et al., 2015, 2016), with the sub-polar and polar VMRs becoming larger than the equatorial and mid-latitude bins. The lack of measurements at low altitudes in the mid-latitude and equatorial bins prevents comparison with the higher-latitude bins. These results are also seen on the map of the mean CO VMR as a function of the latitude and pressure in Panel F.

In Panels D and E, the mean CO profiles from this work are compared with those obtained in the previous version of the dataset presented in Vandaele et al. (2015, 2016). The changes to the code and the spectral data between the two versions are listed in Section 4.2. The new CO number densities in Panel D are an order of magnitude smaller than the previously obtained values, with larger differences observed for absolute latitudes smaller than 80°. In Panel F, the CO VMRs are larger by a factor

of up to 2 compared to the previous version, mostly above 10^{-3} mbar/~110 km. The CO VMR profiles are also compared with literature values (Clancy, 2016; Gurwell et al., 1995; Krasnopolsky, 2008; Krasnopolsky, 2012; Lellouch et al., 1994; Marcq et al., 2005) and are in very good agreement, except for the Clancy profile above 10^{-2} mbar/~98 km, probably due to the difference in measurement geometry (the Clancy profiles are measurements from ground-based telescopes taken in nadir).

4.5. Water vapour

Water vapour and its main isotopologue HDO were recently studied by Chamberlain et al. (2020) for H_2O and Mahieux et al. (2023b) for HDO and the HDO/H_2O ratio. The water vapour database presented in this work is the same as the one discussed in these two papers, and it is only presented here for the sake of completeness. We refer the readers to these papers for a deeper discussion of the data. The values for the densities and VMRs provided in this work correspond to the concentrations of the isotopologue only. Fig. 3 Panel C shows the location of the H_2O observations, and Panel D of the same figure the location of the observations of HDO.

In Fig. 7 and Fig. 8, Panels A are the individual number densities. Panels B shows the mean density profile for the morning and evening as a function of the pressure considering only observations that took place between −60° and 60°, and Panels C the corresponding VMRs. Panels D are the mean densities for the latitude bins (0°-30°, 30°-60°, 60°-80°, and 80°-90°), and Panels E is the corresponding VMRs. In Panels B to E, the coloured envelopes depict the variabilities corresponding to the 1-σ standard deviations of the number densities logarithm of the individual profiles considered on a pressure scale. Finally, Panels F of both Figures show a map (latitude vs pressure) of the mean latitudinal profiles.

The uncertainties are not displayed in Fig. 7 Panel A for clarity; they vary from 40% at 120 km to 14% at 100 km and increase to 50% below 80 km. The variability, computed as the 1-σ standard deviation of the logarithm of the individual profiles considered on a pressure scale, varies from a factor of 0.5 at 10^{-4} mbar/~118 km, increasing linearly to 1.5 at 1 mbar/~80 km and decreases to a factor 0.5 at 10 mbar/~74 km.

From Panel C, we see that the water vapour VMR is larger in the morning than in the evening, by a factor of 1.02 at 6×10^{-4} mbar/~112 km and up to a factor of 1.6 at 0.12 mbar/~86 km.

The VMR profiles for the different latitude bins as a function of the pressure also vary. At the 6×10^{-4} mbar/~112 km, the mid-latitude (30°-60°), subpolar (60°-80°), and polar (80°-90°) are smaller than the equatorial profile (0°-30°) by 20%, 24%, and 46%, respectively. In the 5×10^{-3} mbar/~101 km to 10^{-3} mbar/~98 km region, the four profiles have very similar values within 10%. Below 10^{-3} mbar/~98 km pressure level, the water vapour amount is smaller in the equatorial bin than in the others. At 0.1 mbar/~87 km, the equatorial bin is smaller by 28% (mid-latitude) and 71% (subpolar and polar). Lower, no equatorial values are available; the mid-latitude VMRs are smaller than the polar ones by 40%, while the subpolar VMRs are larger by up to 60% than the polar ones. This is reflected in the VMR map as a function of latitude and pressure given in Fig. 7.

The HDO individual profiles from Fig. 8 Panel A have uncertainties varying between 50% at 110 km and 15% between 90 and 70 km. The HDO variability varies between a factor of 0.4 and 0.7, thus much lower than the variability of H_2O. The mean local solar time number density profiles in Panel B and the corresponding VMRs profiles in Panel C show that the evening profiles are always smaller than the morning ones by a factor of 1.2 at 0.4 mbar/~83 km, like what was obtained for H_2O.

Finally, the mean profiles per latitude bin are plotted in Panels D (density profiles) and E (VMRs). The mean profiles show much lower differences as a function of latitude than the H_2O profiles, as can be inferred from Panel F, showing a map of the variations of the HDO VMR as a function of latitude and pressure. This specific aspect of the HDO and H_2O profiles will be discussed in a coming publication.

4.6. Hydrochloric acid

This Section is an update to the previous work of Mahieux et al. (2015c). That work focused on 180 observations of $H^{35}Cl$ and $H^{37}Cl$; here, we present 405 observations of $H^{35}Cl$ and 394 of $H^{37}Cl$. The locations of the observations are given in Fig. 3 Panels E and F.

SOIR could detect two isotopologues of HCl: $H^{35}Cl$ and $H^{37}Cl$. They are presented separately in this Section, while the HITRAN line intensities have been multiplied by the Earth's isotopic abundance as reported in HITRAN, i.e. 0.7576 and 0.2423, such that the derived number density profiles and associated VMRs refer to the isotopologue itself. $D^{35}Cl$ and $D^{37}Cl$ also absorb in the SOIR wavenumber range, but their spectral signatures are very close to the SOIR detection limit, i.e. their signatures are very close to the noise level. A special procedure like the one used in Mahieux et al. (2023) will be set up in a coming publication, which is outside of this work's scope.

Panels A in Fig. 9 and Fig. 10 display the individual profiles of $H^{35}Cl$ and $H^{37}Cl$. The uncertainties are not displayed for clarity and are equal to 20% at 110 km up to 100% at 70 km for $H^{35}Cl$ and 25% from 115 to 90 km and increasing to 80% at 70 km for $H^{37}Cl$. The variability varies from a factor 0.5 in the 10^{-4} mbar/~120 km to 0.1 mbar/~87 km region to a factor 2 at 1 mbar/~80 km down to a factor 0.5 at 10 mbar/~74 km for $H^{35}Cl$. $H^{37}Cl$ varies from 0.5 above 0.04 mbar/~93 km up to a factor 3 at 25 mbar/~70 km.

The evening and morning mean number density profiles are displayed in Panels B of Fig. 9 and Fig. 10, and in Panels C, their equivalent VMR profiles are provided. These profiles only consider observations taken at absolute latitudes lower than 60°. For both isotopologues, the VMR profiles both show a constant slope on a logarithmic scale varying from 134 ppb for $H^{35}Cl$ and 58 ppb for $H^{37}Cl$ at 0.5 mbar/~83 km to 0.96 ppm for $H^{35}Cl$ and 0.62 ppm for $H^{37}Cl$ at 4×10^{-3} mbar/~104 km. The morning and evening profiles are nearly equal, with the morning $H^{35}Cl$ VMR profile being 70% of the evening one at 10^{-3} mbar/~110 km and 115% at 0.1 mbar/~87 km. The morning $H^{37}Cl$ VMR profile is 80% of the morning one at 4×10^{-3} mbar/~104 km and increases to 130% at 0.16 mbar/~86 km.

Panels D of Fig. 9 and Fig. 10 show the mean number density profiles for the different latitude bins. The $H^{35}Cl$ and $H^{37}Cl$ VMR profiles displayed in Panels E of the two figures for the latitude bins are very similar in the 2×10^{-4} mbar/~117 km to 4×10^{-2} mbar/~92 km, showing a constant increasing slope on a logarithmic scale with increasing altitude. The polar (80°-90°), subpolar (60°-80°), and mid-latitudes (30°-60°) profiles then show a minimum at approx. 0.2 mbar/~85 km with a value of 0.26 ppm for both isotopologues. They increase with decreasing altitude to the bottom of the profile at 10 mbar/~74 km. However, the equatorial (0°-30°) mean profile shows a constant decreasing slope down to 0.4 mbar/~84 km and a value of 86 ppb for $H^{35}Cl$ and 61 ppb at 0.3 mbar/~85 km for $H^{37}Cl$.

They are compared to the mean VMR profiles from Mahieux et al. (2015c), where the VMRs are scaled by the Earth's isotopic ratio to be comparable to the values reported in both Panels. The latitude bin VMR profiles show different shapes than the profiles of Mahieux et al. (2015c). They are also compared to literature profiles (Iwagami et al., 2008; Sandor and Clancy, 2012; Young, 1972; Yung and DeMore, 1982) in Panels E, where the profiles and values reported in those works were multiplied by the isotopic factor of 0.7576 in Fig. 9 and 0.2423 in Fig. 10. They show a very good agreement with the mean latitude profiles of bins 30°-60°, 60°-80°, and 80°-90° reported in this work. The VMR in the 0°-30° latitude bin shows decreasing concentrations with decreasing altitude in the 0.1 mbar/~87 km to 0.3 mbar/~83 km, whereas the other bins show an inversion of the concentration at those altitudes.

Finally, the mean profiles are plotted as maps (latitude vs. pressure) in Panels F of Fig. 9 and Fig. 10.

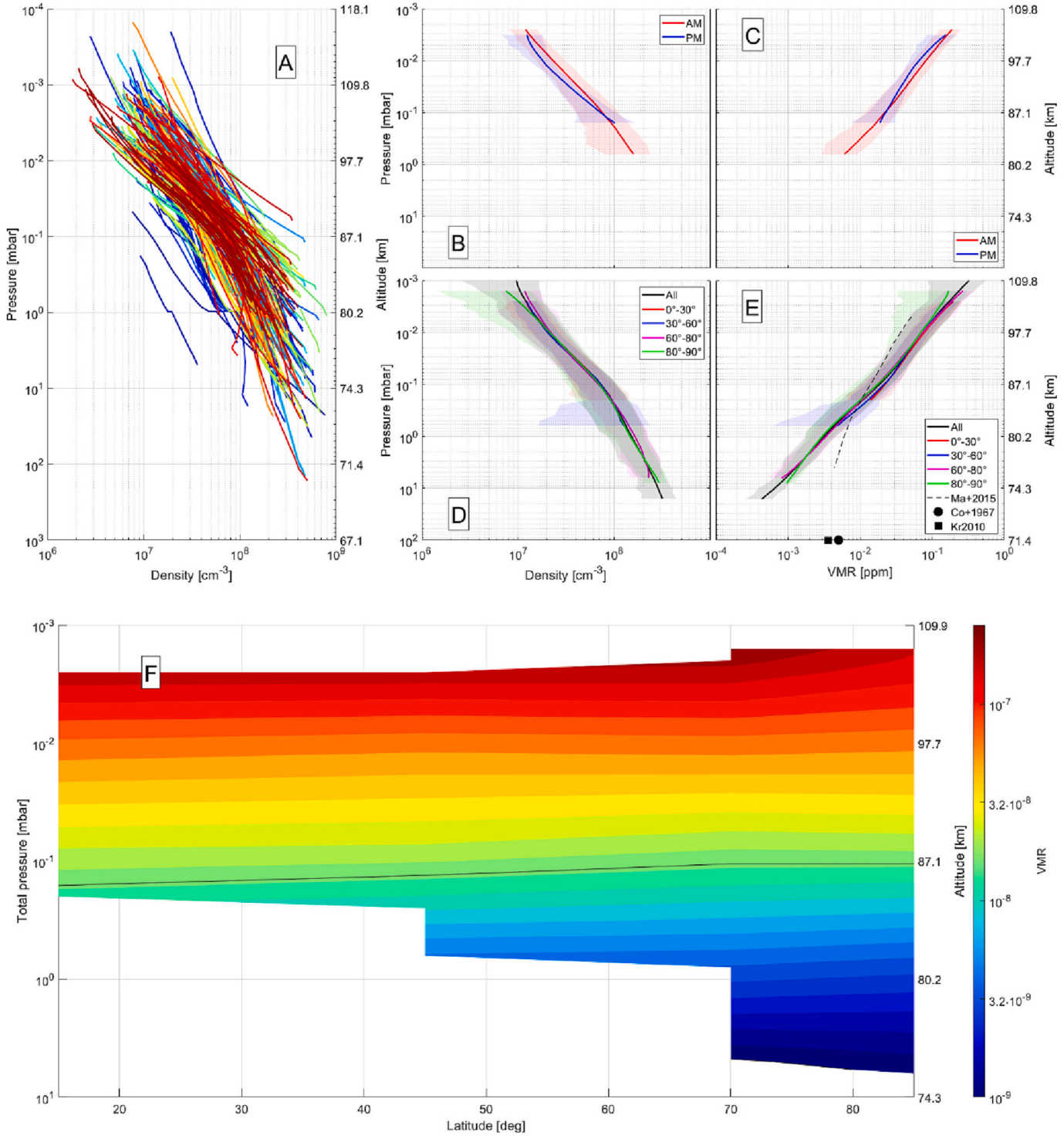

Fig. 11. (Panel A) Individual retrieved HF number density profiles as a function of the altitude. The colour code is the time, from blue for 2006 observations to red for the 2014 ones. (Panel B) Mean HF number density profiles for the morning (red) and evening profiles (blue). (Panel C) Mean VMR of the profiles plotted in Panel B. (Panel D) Mean HF number density profiles for the whole database (black), for 0°-30° latitude observations (red), 30°-60° (blue), 60°-80° (magenta), and 80°-90° (green). Equatorial symmetry is assumed between the Northern and Southern hemispheres. (Panel E) Mean VMR of the profiles plotted in Panel D. (Panel F) Map of the mean HF VMR as a function of the pressure and the absolute latitude. In Panels B and C, the envelopes show the variability, and in Panels C, E, and F, the approximate altitude is given on the right-hand side of the plots. In Panel E, the dashed line is the mean VMR vertical profile from Mahieux et al. (2015c). The dots correspond to the values found in the literature at the cloud top, with "Co + 1967" corresponding to Connes et al. (1967) and "Kr2010" to Krasnopolsky (2010b).(For interpretation of the references to color in this figure legend, the reader is referred to the web version of this article.)

4.7. Hydrofluoric acid

This Section is an update to the previous work by Mahieux et al. (2015c) on HF. That work presented partial results of the SOIR database, with 44 orbits considered; in this work, we present the results of 284 observations. The location of the occultations is given in Fig. 3 Panel G.

Fig. 11 Panel A shows the individual number density profiles from the SOIR database. The uncertainties are not displayed for clarity, and they vary from 20 to 45%. The variability is smaller on the whole pressure/altitude range than for the other species: it varies from a factor 0.4 to 0.5 in the 10^{-3} mbar/~110 km to 10^{-2} mbar/~98 km and 0.07 mbar/~90 km to 4 mbar/~77 km and is equal to 0.2 in the other regions.

Panel B shows the mean number density profiles for the morning and evening observations at absolute latitudes lower than 60°, and Panel C the corresponding VMR profiles. Both VMR profiles are very similar and show an increasing constant slope on a logarithmic scale, from 6 ppb at 0.6 mbar/~82 km to 0.19 ppm at 2.5×10^{-3} mbar/~105 km. The morning average profile is up to 30% larger than the evening one.

In Panel D, the number density profiles for the different latitude bins are nearly equal, showing the same slope as the mean AM and PM profiles. In Panel E, the minimum value equals 0.4 ppb at 15 mbar/~73 km, and the maximum is 0.32 ppm at 10^{-3} mbar/~110 km. The steadiness with latitude can be assessed in Panel F, which shows a map of the HF *V*MR as a function of the pressure and the latitude. In Panel E, the few HF measurements from the literature taken at the cloud top are also displayed (Connes et al., 1967; Krasnopolsky, 2010b). In this work, the profiles do not go down to the cloud top, where the literature values were measured. They have similar values to the ones we find at 1 mbar/~80 km.

5. Conclusions

In this work, we present an update of the previously published databases (Chamberlain et al., 2020; Mahieux et al., 2015a; Mahieux et al., 2012; Mahieux et al., 2015c; Vandaele et al., 2015, 2016) on CO_2, CO, H_2O, HDO, $H^{35}Cl$, $H^{37}Cl$, and HF from the SOIR on board Venus Express measurements following an improvement of the calibrated transmittance pipeline (Trompet et al., 2016) and updates to the ASIMAT retrieval code. The H_2O and HDO profiles are the same as the ones published in Chamberlain et al. (2020) and Mahieux et al. (2023b), as they were obtained using the same code version as the one used in this work. The latest concerns:

(1) A more reliable computation of the temperature profiles from the CO_2 number density profiles by considering an upper-boundary condition to the hydrostatic equation partial derivative equation as isothermal instead of fixing the temperature at the top.
(2) Better accounting of the information from the averaging kernels to decide which measurements were actually fitted. More orders were also considered for detecting CO_2, H_2O, HDO, and HCl.
(3) More observations are presented for each species.

We present the individual profile database and compute on a pressure scale the mean profiles and associated variability of each species as a function of the side of the terminator for absolute latitudes lower than 60° and mean latitudinal profiles (for bins at 0°-30°, 30°-60°, 60°-80°, and 80°-90°) assuming side of the terminator and equatorial symmetries. The mean profiles are compared with the previously published SOIR profiles and compared with the literature; they generally show a better agreement:

- The mean CO_2 profiles show weak latitudinal and side of the terminator dependency, with lower number density from the previous version (Mahieux et al., 2015a) by a factor up to 10.
- The mean temperature profiles show, as in the previous version of the database (Mahieux et al., 2015a), a succession of minima and maxima, slightly displaced in intensity and altitude.
- The mean CO volume mixing ratio (VMR) profiles have lower values than in the previous version and are still in good agreement with the literature.
- The HCl profiles are now in much better agreement with the literature.
- The H_2O profiles show dependence as a function of the latitude bin, while the HDO profiles do not, as Fedorova et al. (2016) observed.
- The HF profiles are similar as a function of the side of the terminator and latitude bins and show a constant slope in logarithm from the cloud top to ~100 km.

The mean values and variabilities of all the mean profiles discussed in this work are provided in Appendix C, Table 4 to Table 11.

All the profiles are available on the *V*irtual European Solar and Planetary Access (VESPA) at https://vespa-client-dev.obspm.fr/planetary/data/ and are described in Trompet et al. (2018).

Declaration of Competing Interest

The authors declare that they have no known competing financial interests or personal relationships that could have appeared to influence the work reported in this paper.

Data availability

The data are available on the ESA PSA repository and on the VESPA platform, as described in the text.

Acknowledgments

Venus Express is a planetary mission from the European Space Agency (ESA). We wish to thank all ESA members who participated in the mission, particularly H. Svedhem and D. Titov. We thank our collaborators at IASB-BIRA (Belgium), Latmos (France), and IKI (Russia). We thank CNES, CNRS, Roskosmos, and the Russian Academy of Science. The research program was supported by the Belgian Federal Science Policy Office and the European Space Agency (ESA, PRODEX program, contracts C 90268, 90113, and 17645). We acknowledge the support of the “Interuniversity Attraction Poles” program financed by the Belgian government (Planet TOPERS). The research leading to these results has received funding from the European Union Seventh Framework Program (FP7/2007-2013) under grant agreement n°606798. A. Mahieux was supported by the Marie Skłodowska-Curie Action from the European Commission under grant number 838587. S. Robert thanks BELSPO for the FED-tWIN funding (Prf-2019-077 - RT-MOLEXO).

Appendix A. Supplementary data

Supplementary data to this article can be found online at https://doi.org/10.1016/j.icarus.2023.115713.

References

Arney, G., Meadows, V., Crisp, D., Schmidt, S.J., Bailey, J., Robinson, T., 2014. Spatially resolved measurements of H_2O, HCl, CO, OCS, SO_2, cloud opacity, and acid concentration in the Venus near-infrared spectral windows. J. Geophys. Res.: Planets 119, 1860–1891.

Belyaev, D., et al., 2012. Vertical profiling of SO2 and SO above Venus' clouds by SPICAV/SOIR solar occultations. Icarus. 217, 740–751.

Belyaev, D., et al., 2016. Distribution of SO_2 content at the night side of Venus' upper mesosphere. International Venus conference. Oxford, UK, 4-8 April,, pp. 12–13. https://venus2016.files.wordpress.com/2016/02/venus2016_abstracts_sorted_by_author.pdf.

Belyaev, D.A., et al., 2017. Night side distribution of SO2 content in Venus' upper mesosphere. Icarus. 294, 58–71.

Bertaux, J.L., et al., 2007a. SPICAV on Venus Express: three spectrometers to study the global structure and composition of the Venus atmosphere. Planet. Space Sci. 55, 1673–1700.
Bertaux, J.L., et al., 2007b. A warm layer in Venus' cryosphere and high altitude measurements of HF, HCl, H_2O and HDO. Nature. 450, 646–649.
Chamberlain, S., et al., 2020. SOIR/VEx observations of water vapor at the terminator in the Venus mesosphere. Icarus. 346, 113819.
Clancy, R.T., 2016. Personal communication.
Clancy, R.T., Sandor, B.J., Moriarty-Schieven, G., 2003. Observational definition of the Venus mesopause: vertical structure, diurnal variation, and temporal instability. Icarus. 161, 1–16.
Clancy, R.T., Sandor, B., Moriarty-Schieven, G., 2012. Thermal structure and CO distribution for the Venus mesosphere/lower thermosphere: 2001–2009 inferior conjunction sub-millimeter CO absorption line observations. Icarus. 217, 779–793.
Connes, P., Connes, J., Benedict, W.S., Kaplan, L., 1967. Traces of HCl and HF in the atmosphere of Venus. Astrophys. J. 147, 1230–1237.
Cottini, V., Ignatiev, N.I., Piccioni, G., Drossart, P., 2015. Water vapor near Venus cloud tops from VIRTIS-H/Venus Express observations 2006–2011. Planet. Space Sci. 113-114, 219–225.
Donahue, T.M., 1968. The upper atmosphere of Venus: a review. J. Atmos. Sci. 25, 568–573.
Drossart, P., et al., 2007. Scientific goals for the observation of Venus by VIRTIS on ESA/Venus Express mission. Planet. Space Sci. 55, 1653–1672.
Encrenaz, T., Moreno, R., Moullet, A., Lellouch, E., Fouchet, T., 2015. Submillimeter mapping of mesospheric minor species on Venus with ALMA. Planet. Space Sci. 113-114, 275–291.
Encrenaz, T., et al., 2016. HDO and SO_2 thermal mapping on Venus. Astron. Astrophys. 595, A74.
Encrenaz, T., et al., 2020. HDO and SO2 thermal mapping on Venus. A&A. 639, A69.
Fedorova, A., et al., 2008. HDO and H_2O vertical distributions and isotopic ratio in the Venus mesosphere by solar occultation at infrared spectrometer onboard Venus Express. J. Geophys. Res. 113, E00B22.
Fedorova, A.A., Marcq, E., Luginin, M., Korablev, O., Bertaux, J.L., Montmessin, F., 2016. Variations of water vapor and cloud top altitude in the Venus' mesosphere from SPICAV/VEx observations. Icarus. 275.
Gilli, G., 2012. Carbon monoxide and temperature in the upper atmosphere of Venus through the analysis of limb observations by VIRTIS/Venus Express. INSTITUTO DE ASTROF'ISICA DE ANDALUC'IA, Vol. PhD thesis. Universidad de Granada, Granada.
Gilli, G., et al., 2015. Carbon monoxide and temperature in the upper atmosphere of Venus from VIRTIS/Venus Express non-LTE limb measurements. Icarus. 248, 478–498.
Gurwell, M., Muhleman, D.O., Shah, K., Berge, G., Rudy, D.J., Grossman, A.W., 1995. Observations of the CO bulge on Venus and implications for mesospheric winds. Icarus. 115, 141–158.
Hedin, A.E., Niemann, H.B., Kasprzak, W.T., 1983. Global empirical model of the Venus thermosphere. J. Geophys. Res. 88, 73–83.
Iwagami, N., et al., 2008. Hemispheric distributions of HCl above and below the Venus' clouds by ground-based 1.7 μm spectroscopy. Planet. Space Sci. 56, 1424–1434.
Jessup, K.L., et al., 2015. Coordinated Hubble space telescope and Venus Express observations of Venus' upper cloud deck. Icarus. 258, 309–336.
Krasnopolsky, V.A., 2008. High-resolution spectroscopy of Venus: detection of OCS, upper limit to H2S, and latitudinal variations of CO and HF in the upper cloud layer. Icarus. 197, 377–385.
Krasnopolsky, V., 2010a. Spatially-resolved high-resolution spectroscopy of Venus 2. Variations of HDO, OCS, and SO_2 at the cloud tops. Icarus. 209, 314–322.
Krasnopolsky, V.A., 2010b. Spatially-resolved high-resolution spectroscopy of Venus. 1. Variations of CO2, CO, HF, and HCl at the cloud tops. Icarus. 208, 539–547.
Krasnopolsky, V.A., 2012. A photochemical model for the Venus atmosphere at 47-112 km. Icarus. 218, 230–246.
Krasnopolsky, V.A., Belyaev, D.A., Gordon, I.E., Li, G., Rothman, L.S., 2013. Observations of D/H ratios in H2O, HCl, and HF on Venus and new DCl and DF line strengths. Icarus. 224, 57.
Lellouch, E., Goldstein, J., Rosenqvist, J., Bougher, S.W., Paubert, G., 1994. Global circulation, thermal structure and carbon monoxide distribution in Venus' mesosphere in 1991. Icarus. 110, 315–339.
Limaye, S., et al., 2017. The thermal structure of the Venus atmosphere: Intercomparison of Venus Express and ground based observations of vertical temperature and density profiles. Icarus. 294, 124–155.
Limaye, S.S., Grassi, D., Mahieux, A., Migliorini, A., Tellmann, S., Titov, D., 2018. Venus atmospheric thermal structure and radiative balance. Space Sci. Rev. 214, 102.
Luginin, M., Fedorova, A., Belyaev, D., Montmessin, F., Korablev, O., Bertaux, J.L., 2018. Scale heights and detached haze layers in the mesosphere of Venus from SPICAV IR data. Icarus. 311, 87–104.
Mahieux, A., et al., 2008. In-flight performance and calibration of SPICAV/SOIR on-board Venus Express. Appl. Opt. 47, 2252–2265.
Mahieux, A., Wilquet, V., Drummond, R., Belyaev, D., Fedorova, A., Vandaele, A.C., 2009. A new method for determining the transfer function of an Acousto optical tunable filter. Opt. Express 17, 2005–2014.
Mahieux, A., et al., 2010. Densities and temperatures in the Venus mesosphere and lower thermosphere retrieved from SOIR onboard Venus Express: retrieval technique. J. Geophys. Res. 115.
Mahieux, A., et al., 2012. Densities and temperatures in the Venus mesosphere and lower thermosphere retrieved from SOIR on board Venus Express: carbon dioxide measurements at the Venus terminator. J. Geophys. Res. 117, E07001.
Mahieux, A., et al., 2015a. Update of the Venus density and temperature profiles at high altitude measured by SOIR on board Venus Express. Planet. Space Sci. 113-114, 309–320.
Mahieux, A., et al., 2015b. Venus mesospheric sulfur dioxide measurement retrieved from SOIR on board Venus Express. Planet. Space Sci. 113-114, 193–204.
Mahieux, A., Wilquet, V., Vandaele, A.C., Robert, S., Drummond, R., Bertaux, J.L., 2015c. Hydrogen halides measurements in the Venus upper atmosphere retrieved from SOIR on board Venus Express. Planet. Space Sci. 113-114, 264–274.
Mahieux, A., et al., 2023. Update on SO2, detection of OCS, CS, CS2, and SO3, and upper limits of H2S and HOCl in the Venus mesosphere using SOIR on board Venus Express. Icarus. 399, 115556.
Marcq, E., Bézard, B., Encrenaz, T., Birlan, M., 2005. Latitudinal variations of CO and OCS in the lower atmosphere of Venus from near-infrared nightside spectro-imaging. Icarus. 179, 375–386.
Marcq, E., Bézard, B., Drossart, P., Piccioni, G., Reess, J.M., Henry, F., 2008. A latitudinal survey of CO, OCS, H_2O, and SO_2 in the lower atmosphere of Venus: spectroscopic studies using VIRTIS-H. J. Geophys. Res. 113 https://doi.org/10.1029/2008JE003074.
Marcq, E., Mills, F.P., Parkinson, C.D., Vandaele, A.C., 2018. Composition and chemistry of the neutral atmosphere of Venus. Space Sci. Rev. 214, article 10.
Mills, F.P., Allen, M., 2007. A review of selected issues concerning the chemistry in Venus' middle atmosphere. Planet. Space Sci. 55, 1729–1740.
Montmessin, F., et al., 2011. A layer of ozone detected in the nightside upper atmosphere of Venus. Icarus. 216, 82–85.
Moroz, V.I., 1981. The atmosphere of Venus. Space Sci. Rev. 29, 3–127.
Nevejans, D., et al., 2006. Compact high-resolution space-borne echelle grating spectrometer with AOTF based on order sorting for the infrared domain from 2.2 to 4.3 micrometer. Appl. Opt. 45, 5191–5206.
Oschlisniok, J., et al., 2021. Sulfuric acid vapor and sulfur dioxide in the atmosphere of Venus as observed by the Venus Express radio science experiment VeRa. Icarus. 362, 114405.
Piccialli, A., et al., 2012. Dynamical properties of the Venus mesosphere from the radio-occultation experiment VeRa onboard Venus Express. Icarus. 217, 669–681.
Piccialli, A., et al., 2015. Thermal structure of Venus upper aymosphere measured by stellar occultations with SPICAV/Venus Express. Planet. Space Sci. 113-114, 321–335.
Rodgers, C.D., 2000. Inverse Methods for Atmospheric Sounding: Theory and Practice. University of Oxford.
Rothman, L.S., et al., 2013. The HITRAN2012 molecular spectroscopic database. J. Quant. Spectrosc. Radiat. Transf. 130, 4.
Sandor, B., Clancy, R.T., 2012. Observations of HCl altitude dependence and temporal variation in the 70-100 km mesosphere of Venus. Icarus. 220, 618–626.
Sandor, B., Clancy, R.T., 2017. Diurnal observations of HCl altitude variation in the 70–100 km mesosphere of Venus. Icarus. 290, 156–161.
Seiff, A., et al., 1980. Measurements of thermal structure and thermal contrasts in the atmosphere of Venus and related dynamical observations: results from the four Pioneer Venus probes. J. Geophys. Res. 85, 7903–7933.
Taylor, F.W., 2006. Venus before Venus Express. Planet. Space Sci. 54, 1249–1262.
Taylor, F.W., et al., 1980. Structure and meteorology of the middle atmosphere of Venus: infrared remote sensing from the Pioneer orbiter. J. Geophys. Res. 85, 7963–8006.
Tellmann, S., et al., 2012. Small-scale temperature fluctuations seen by the VeRa radio science experiment on Venus Express. Icarus. 221, 471–480.
Titov, D.V., et al., 2006. Venus express science planning. Planet. Space Sci. 54, 1279–1297.
Trompet, L., et al., 2016. Improved algorithm for the transmittance estimation of spectra obtained with SOIR/Venus Express. Appl. Opt. 55, 9275–9281.
Trompet, L., et al., 2018. Description, accessibility and usage of SOIR/Venus Express atmospheric profiles of Venus distributed in VESPA (virtual European solar and planetary access). Planet. Space Sci. 150, 60–64.
Tsang, C.C.C., et al., 2009. Variability of CO concentrations in the Venus troposphere from Venus Express/VIRTIS using a band ratio technique. Icarus. 201, 432–443.
Vandaele, A.C., Mahieux, A., Robert, S., Drummond, R., Wilquet, V., Bertaux, J.L., 2015. Carbon monoxide short term variability observed on Venus with SOIR/VEX. Planet. Space Sci. 113-114, 237–255.
Vandaele, A.C., et al., 2016. Carbon monoxide observed in Venus' atmosphere with SOIR/VEx. Icarus. 272, 48–59.
Young, L., 1972. High resolution spectra of Venus: a review. Icarus. 17, 632–658.
Yung, Y.L., DeMore, W.B., 1982. Photochemistry of the stratosphere of Venus: implications for atmospheric evolution. Icarus. 51, 199–247.
Zasova, L.V., Moroz, V.I., Linkin, V.M., Khatountsev, I.A., Maiorov, B.S., 2006. Structure of the Venusian atmosphere from surface up to 100 km. Cosm. Res. 44, 364–383.